ARTICLES
https://doi.org/10.1038/s41567-022-01603-1

nature physics

Spin-excitation anisotropy in the nematic state of detwinned FeSe

Xingye Lu[1]✉, Wenliang Zhang[2], Yi Tseng[2], Ruixian Liu[1], Zhen Tao[1], Eugenio Paris[2], Panpan Liu[1], Tong Chen[3], Vladimir N. Strocov[2], Yu Song[4], Rong Yu[5], Qimiao Si[3], Pengcheng Dai[3]✉ and Thorsten Schmitt[2]✉

The origin of the electronic nematicity in FeSe is one of the most important unresolved puzzles in the study of iron-based superconductors. In both spin- and orbital-nematic models, the intrinsic magnetic excitations at $\mathbf{Q}_1 = (1, 0)$ and $\mathbf{Q}_2 = (0, 1)$ of twin-free FeSe are expected to provide decisive criteria for clarifying this issue. Although a spin-fluctuation anisotropy below 10 meV between $\mathbf{Q}_1$ and $\mathbf{Q}_2$ has been observed by inelastic neutron scattering at low temperature, it remains unclear whether such an anisotropy also persists at higher energies and associates with the nematic transition T_s. Here we use resonant inelastic X-ray scattering to probe the high-energy magnetic excitations of detwinned FeSe. A prominent anisotropy between the magnetic excitations along the *H* and *K* directions is found to persist to $E \approx 200$ meV, which decreases gradually with increasing temperature and finally vanishes at a temperature around T_s. The measured high-energy spin excitations are dispersive and underdamped, which can be understood from a local-moment perspective.Taking together the large energy scale far beyond the d_{xz}/d_{yz} orbital splitting, we suggest that the nematicity in FeSe is probably spin-driven.

Intertwined order and fluctuations in high-transition-temperature (T_c) superconductors are pivotal for understanding the microscopic origin of superconducting electron pairing[1]. Of particular interest is the electronic nematic state present in both cuprate and iron-based superconductors (FeSCs). Initially discovered through in-plane electronic anisotropy with C_2 symmetry in the paramagnetic orthorhombic state of detwinned $Ba(Fe_{1-x}Co_x)_2As_2$ (refs. [2–4]), the electronic nematic state (and its fluctuations) has been identified as a ubiquitous feature of FeSCs and is believed to be essential for the structural and magnetic transitions in FeSCs (refs. [5–9]), and may enhance the electron pairing for high-T_c superconductivity[10–12].

Iron selenide (FeSe) is a unique material among FeSCs because of its simple structure (Fig. 1a)[13] and unusual electronic properties, such as strong anisotropy of the superconducting order parameter, extended electronic nematic phase and highly tunable T_c (ref. [9]). In particular, unlike iron pnictide, which has a collinear antiferromagnetic (AF) ground state below the tetragonal-to-orthorhombic structural (nematic) phase transition T_s, although FeSe exhibits a similar nematic transition ($T_s \approx 90$ K)[14], it has no static AF order, providing a broad temperature range below T_s as an ideal platform for investigating electronic nematicity and its interplay with superconductivity.

FeSe consists of stacked charge-neutral FeSe layers (Fig. 1a). On cooling, it undergoes a nematic transition at $T_s \approx 90$ K, below which twin domains form along two mutually perpendicular directions and exhibit macroscopic four-fold symmetry, impeding the study of the intrinsic electronic properties of the orthorhombic (nematic) state. Through detwinning of FeSe using uniaxial strain, resistivity and electronic structure measurements reveal strong electronic anisotropy in the nematic state[15,16]. At lower temperature, FeSe enters a superconducting ground state with $T_c \approx 9$ K, in which a superconducting energy gap anisotropy has been observed via angle-resolved photoemission spectroscopy (ARPES)[17–19] and scanning tunnelling spectroscopy[20].

In the presence of orbital splitting (or orbital ordering) between d_{xz} and d_{yz} orbitals[16,21,22], and the absence of magnetic order, the electronic nematic phase has been suggested to be driven by orbital fluctuations[23–26]. On the other hand, experimental evidence, in particular the discovery of intense magnetic excitations and their correlation with the nematic transition[27–29], has emphasized the importance of the spin degree of freedom in driving electronic nematic order. In addition, various localized models based on quantum paramagnetism, spin frustration and magnetic quadrupolar order have been proposed to account for the nematic transition, magnetic excitations and the absence of AF order[30–33].

It is proposed that resolving the intrinsic magnetic excitations in twin-free FeSe is key to clarifying the microscopic origin of the unusual electronic anisotropy in both the superconducting and nematic states[5,6,34]. By employing $BaFe_2As_2$ as a substrate for applying uniaxial strain, some of us have recently measured low-energy spin fluctuations ($E \lesssim 10$ meV) of detwinned FeSe using inelastic neutron scattering[35]. These results have revealed anisotropic spin fluctuations in the normal state and a spin resonance appearing only at $\mathbf{Q}_1 = (1, 0)$ below T_c, consistent with the picture of orbital-selective Cooper pairing[20,36–38]. However, neutron scattering experiments were unable to determine what happens to the magnetic excitation anisotropy across the nematic transition due to enhanced background scattering from the large aluminium detwinning device on warming to T_s. In addition, the energy scale of the magnetic anisotropy is unknown because the background magnetic scattering from the $BaFe_2As_2$ substrate overwhelms the magnetic signal from FeSe for energies above 10 meV (ref. [35]).

An ideal method to probe the intrinsic magnetic excitations of FeSe is resonant inelastic X-ray scattering (RIXS) at the Fe-L_3 edge

[1]Center for Advanced Quantum Studies, Applied Optics Beijing Area Major Laboratory, and Department of Physics, Beijing Normal University, Beijing, China. [2]Photon Science Division, Swiss Light Source, Paul Scherrer Institut, Villigen PSI, Switzerland. [3]Department of Physics and Astronomy, Rice Center for Quantum Materials, Rice University, Houston, TX, USA. [4]Center for Correlated Matter and Department of Physics, Zhejiang University, Hangzhou, China. [5]Department of Physics, Renmin University of China, Beijing, China. ✉e-mail: luxy@bnu.edu.cn; pdai@rice.edu; thorsten.schmitt@psi.ch

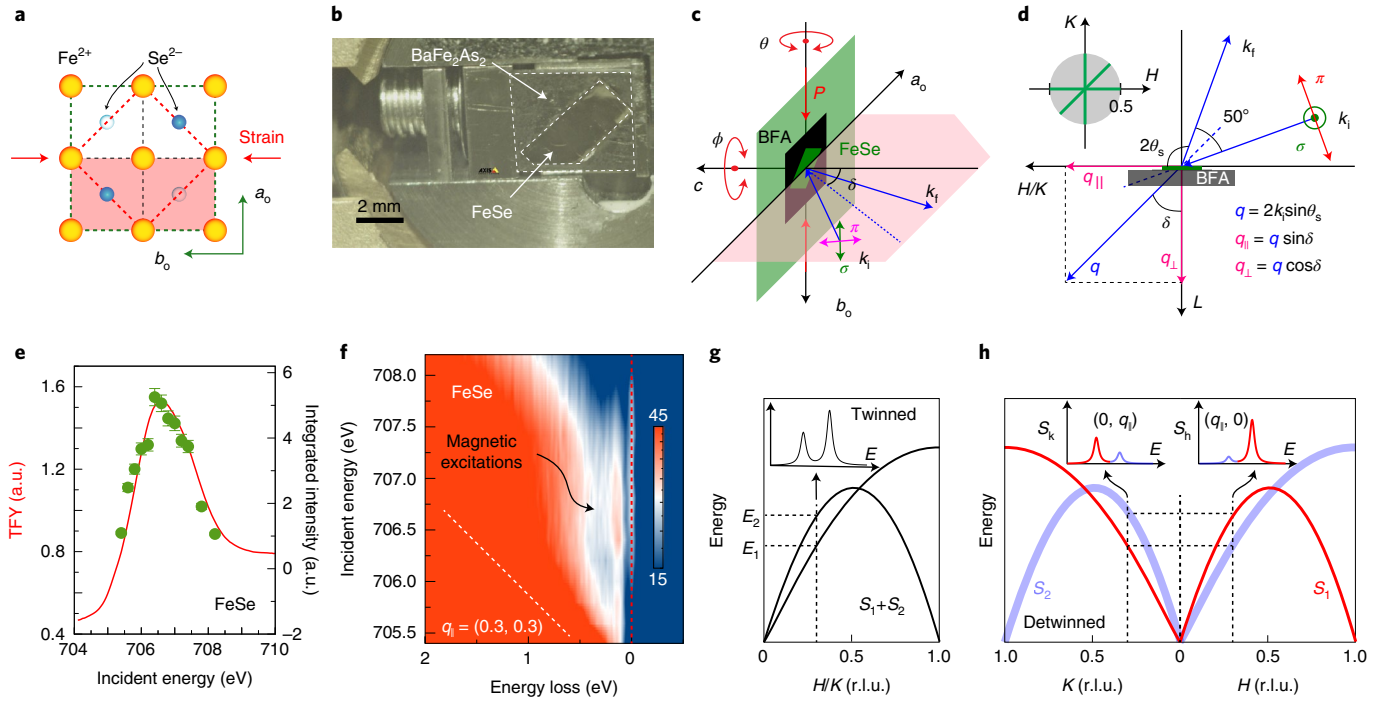

Fig. 1 | Crystal structure, detwinning strategy, scattering geometry and incident energy-dependent RIXS. a, Structure of the FeSe layer. The FeSe crystal consists of stacked FeSe layers. The yellow filled circles represent Fe^{2+} ions. The filled and open blue circles denote Se^{2-} ions above and below the Fe–Fe plane, respectively. The horizontal arrows mark the direction of uniaxial strain. The red dashed diamond and green dashed square denote the tetragonal and orthorhombic unit cells, respectively. **b**, A mechanical detwinning device installed on the RIXS spectrometer, with a thin FeSe crystal glued on a pre-cleaved $BaFe_2As_2$ crystal that is pressured in the device. **c**,**d**, Scattering geometry for RIXS measurements. $\mathbf{q}_{\parallel}$ and $\mathbf{q}_{\perp}$ are projections of $\mathbf{q}$ onto [*H*, *K*] plane and *L* direction. The sample rotation θ around the vertical axis controls the in-plane momentum transfer $q_{\parallel}$ and the rotation ϕ around the *c* axis can tune the scattering plane (pink area) (**c**). The grey filled circle in **d** marks the momentum area accessible in this study ($|\mathbf{q}_{\parallel}| \lesssim 0.5$). The green lines in the grey area in **d** show the high-symmetry directions for RIXS measurements. *P* denotes uniaxial pressure; $k_{i/f}$, initial/final wave vector of photon; and BFA, $BaFe_2As_2$. **e**, The red curve is the total fluorescence yield (TFY) XAS spectrum of FeSe collected near the Fe-L_3 edge (left axis). The green filled circles represent the integrated intensity (right axis) of the magnetic excitations shown in **f**. The error bars in **e** are estimated from the statistics of the data and the 95% confidence interval of the fittings. **f**, Incident-energy dependence of the excitations of FeSe at $\mathbf{q}_{\parallel} = (0.3, 0.3)$, measured near the Fe-$L_3$ edge with π polarization at $T = 20$ K. The magnetic excitations are marked by a curved arrow. **g**,**h**, Schematics of magnetic excitation dispersions for twinned (**g**) and detwinned (**h**) FeSe assuming a difference between spin excitations S_2 and S_1. Correspondingly, the insets in **g** and **h** show schematic RIXS energy spectra for twinned and detwinned FeSe.

in combination with the aforementioned detwinning method (Fig. 1b)[39–44]. RIXS at transition-metal L edges has been widely used to study the (para)magnons of cuprate and FeSCs, as well as various elementary excitations including phonons, crystal-field excitations and plasmons[39–49]. Because Fe-L_3 X-rays (707 eV) penetrate less than 100 nm into FeSe, but the typical thickness of a cleaved FeSe single crystal is ~20 μm, RIXS studies of FeSe are free from signal contamination due to $BaFe_2As_2$ and provide a unique opportunity for measuring high-energy magnetic excitations on detwinned FeSe with high efficiency.

In this Article we use RIXS to measure the intrinsic spin excitations of FeSe and $BaFe_2As_2$ along the high-symmetry directions *H*, *K* and [*H*, *H*], denoted by $S_h(q_{\parallel})$, $S_k(q_{\parallel})$ and $S_{hh}(q_{\parallel})$, respectively (Figs. 2 and 3). To facilitate discussions, we define the spin excitations associated with $\mathbf{Q}_1 = (1, 0)$ as $S_1(\mathbf{q}, E)$ and those associated with $\mathbf{Q}_2 = (0, 1)$ as $S_2(\mathbf{q}, E)$. The ratio between $S_h(q_{\parallel})$ and $S_k(q_{\parallel})$, $\psi(q_{\parallel}) = S_h(q_{\parallel})/S_k(q_{\parallel})$, directly probes the spin-excitation unbalance between S_1 and S_2, which is commonly referred to as nematic spin correlations in the nematic ordering and fluctuating region[34,50,51]. We denote the momentum transfer in reciprocal lattice units (r.l.u.; see Experimental set-ups in the Methods).

Our results reveal that the spin-excitation anisotropy in detwinned FeSe manifests over a large energy range up to 200 meV. It persists up to a temperature slightly above T_s, before fading away at a temperature well above T_s. Its comparison with the intrinsic spin-wave anisotropy of $BaFe_2As_2$ establishes strong nematic spin correlations in both energy scale and amplitude in FeSe. This strong spin-excitation anisotropy builds a direct connection with the nematic phase, suggesting that the nematic order is primarily spin-driven because the energy range of the nematic-phase-induced spin-excitation anisotropy is much larger than that of orbital splitting[22–24]. Furthermore, the RIXS results identify dispersive high-energy spin excitations that are underdamped, which is highly peculiar for a paramagnet, but can be understood from a local-moment-based model with antiferroquadrupolar (AFQ) order[31]. As such, our results provide much needed new insights into the mechanism for the nematicity of FeSe.

Figure 1b shows an FeSe crystal that has been prepared for RIXS measurements, and is glued onto a square-shaped $BaFe_2As_2$ sample with the same orientation. Uniaxial pressure is applied on the $BaFe_2As_2$ along the tetragonal [110] direction (orthorhombic *b* axis). On cooling, the $BaFe_2As_2$ will be detwinned below $T_s \approx 138$ K and generates an orthorhombic distortion $\delta = (a - b)/(a + b) = 0.36\%$ that can be transferred to and thereby detwin FeSe below its structural transition at $T_s \approx 90$ K. Figure 1c,d illustrates the scattering geometry, the substantial area of the first Brillouin zone accessible with Fe-L_3 RIXS, and calculations of the in-plane momenta $q_{\parallel}$.

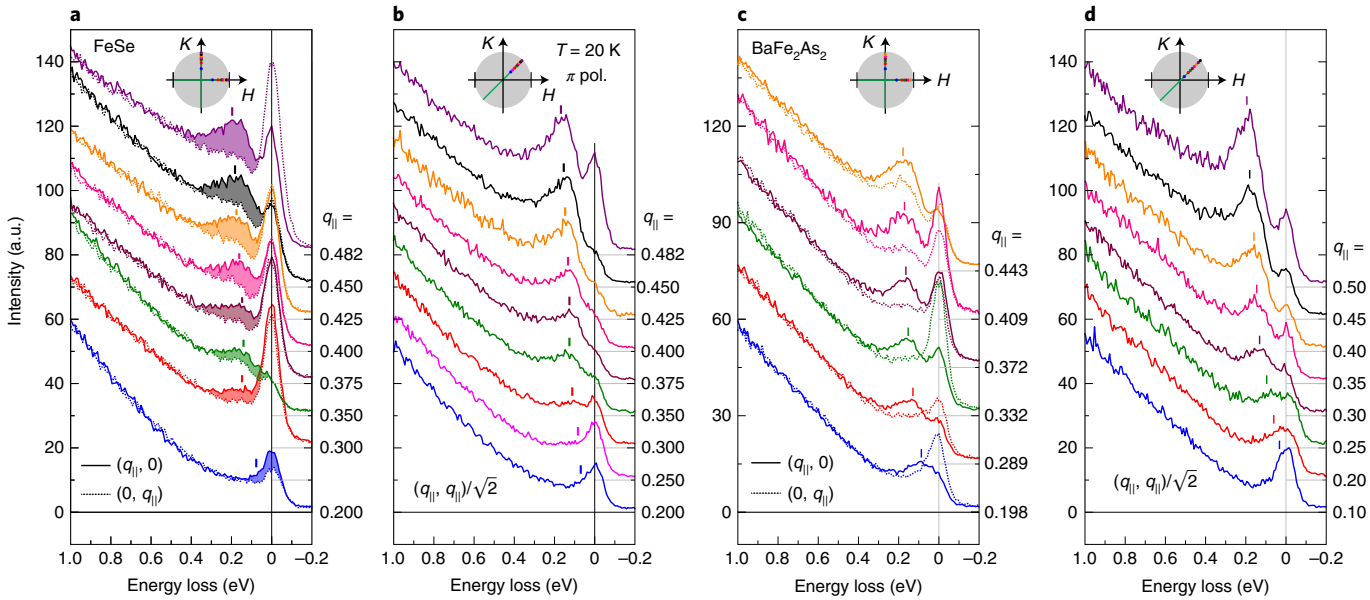

Fig. 2 | Summary of RIXS results on detwinned FeSe and $BaFe_2As_2$. a,**b**, Momentum-dependent RIXS spectra of FeSe along the *H* (solid lines) (**a**) and *K* (dashed lines) directions (**a**) and twinned FeSe along the [*H*, *H*] direction (**b**). The shaded areas mark the difference between $S_h(q_{||})$ and $S_k(q_{||})$. **c**,**d**, Momentum-dependent RIXS spectra of detwinned $BaFe_2As_2$ along the *H*/*K* (**c**) and [*H*, *H*] (**d**) directions. The coloured dots in the insets mark the momenta where spectra were collected.

We first carried out incident-energy-dependent RIXS (energy detuning) measurements for both $BaFe_2As_2$ and FeSe around their resonating energies, which were determined by X-ray absorption spectroscopy (XAS; Fig. 1e and Supplementary Fig. 2). Figure 1f presents a RIXS map for an unstrained FeSe sample measured at $\mathbf{q}_{||} = (0.3, 0.3)$ with π polarization and $T = 20$ K. Although fluorescence and particle–hole excitations dominate the scattering signal above $E \approx 0.5$ eV, a clear intrinsic elementary excitation (Raman mode) is observed at $E \approx 160$ meV that is well separated from the fluorescence peak setting above $E \approx 200$ meV. The integrated intensity of this Raman mode (Fig. 1e, green circles) follows the XAS (Fig. 1e, red curve), indicating that the cross-section is enhanced near the Fe-L_3 edge. In addition, phonon contributions to this mode can also be excluded because of their much smaller energy scale ($E \approx 40$ meV)[43]. Taking together the consistency in energy dispersion between the excitations in Figs. 2 and 3 and those reported in previous studies[39,43,44], we can safely attribute these dispersive excitations to single spin-flip magnetic excitations.

To quantitatively determine the spin-excitation anisotropy in FeSe, we measured the spin excitations of both detwinned FeSe and $BaFe_2As_2$ samples (Figs. 2 and 3), taking the latter as a reference; this can be compared to previous neutron scattering studies of detwinned $BaFe_2As_2$ (ref. [50]). Before discussing the results, we illustrate in Fig. 1g,h the principle for resolving the inherent spin-wave anisotropy and nematic spin correlations in the first Brillouin zone (Supplementary Fig. 3). In a twinned sample with anisotropic excitations, RIXS measurements generate $S_h = S_k$ (black curve in the inset of Fig. 1g). Both S_h and S_k consist of two spin-excitation branches from S_1 and S_2 in twin domains, where we assume S_1 and S_2 have the same energy dispersion for simplicity. For a detwinned sample with local-moment AF order, the spin waves emanate only from the AF vector $\mathbf{Q}_1 = (1, 0)$ ($S_2 = 0$), and S_h/S_k determines the inherent spin-wave anisotropy of S_1. In a detwinned system with nematic spin correlations ($S_1 \neq S_2 \neq 0$), S_1 and S_2 will be present along both *H* and *K* directions (Fig. 2b) with different spectral weight, for which the ratio between S_h and S_k reflects the nematic spin correlations (Supplementary Fig. 3).

Momentum-dependent RIXS spectra of FeSe and $BaFe_2As_2$ collected at $T = 20\,\mathrm{K} < T_s$ are summarized in Fig. 2. In both samples, highly dispersive magnetic excitations along three high-symmetry directions *H*, *K* and [*H*, *H*] are resolved. Figure 2a (2c) displays the intrinsic spin excitations of FeSe ($BaFe_2As_2$) along the *H* and *K* directions, and Fig. 2b (2d) along the [*H*, *H*] direction. Although twinned FeSe and $BaFe_2As_2$ are expected to show four-fold symmetric magnetic excitations[39,52] [$S_h(q_{||}) = S_k(q_{||})$], we find that the detwinned samples exhibit highly anisotropic excitations with $S_h(q_{||}) > S_k(q_{||})$. The substantial difference between $S_h(q_{||})$ and $S_k(q_{||})$ for FeSe persists at all $q_{||}$ measured (Fig. 2a, shaded areas), thus demonstrating the existence of a high-energy spin-excitation anisotropy (nematic spin correlations) in the nematic state of detwinned FeSe. For $BaFe_2As_2$, the spin-excitation anisotropy is a manifestation of the inherent difference in the spin-wave branches along the *H* and *K* directions[50]. The spin-wave anisotropy of $BaFe_2As_2$ increases with $q_{||}$ up to 0.409 but decreases at higher $q_{||} = 0.443$ (Fig. 2c), revealing a non-monotonic momentum dependence. In comparison, the spectral weight difference in FeSe (Fig. 2a, shaded area) retains a large amplitude at an even higher $q_{||} = 0.482$.

To achieve a quantitative characterization of the spin-excitation anisotropy in FeSe and $BaFe_2As_2$, we use a general damped harmonic oscillator model[39–41,43]

$$S(q, E) = A\frac{E_0}{1 - e^{-\beta E}}\frac{2\gamma E}{(E^2 - E_0^2)^2 + (\gamma E)^2} \quad (1)$$

to fit the magnetic excitations, in which E_0 is the undamped energy, γ the damping factor, $\beta = \frac{1}{k_B T}$ (k_B is the Boltzmann constant) and *A* is a fitting coefficient. The elastic peak can be fitted with a Gaussian function, and the fluorescence contributions below $E \approx 1$ eV can be described with a quadratic polynomial (Supplementary Figs. 5 and 6).

The fitting results for FeSe and $BaFe_2As_2$, the undamped energy dispersion ($E_0(q)$), the energies for the intensity maxima ($E_m(q)$) and the damping factor ($\gamma/2$) are summarized in Fig. 3. Figure 3a–c shows a simulation of the spin waves in $BaFe_2As_2$ overlaid by the energy dispersions and the damping factors. The simulation is

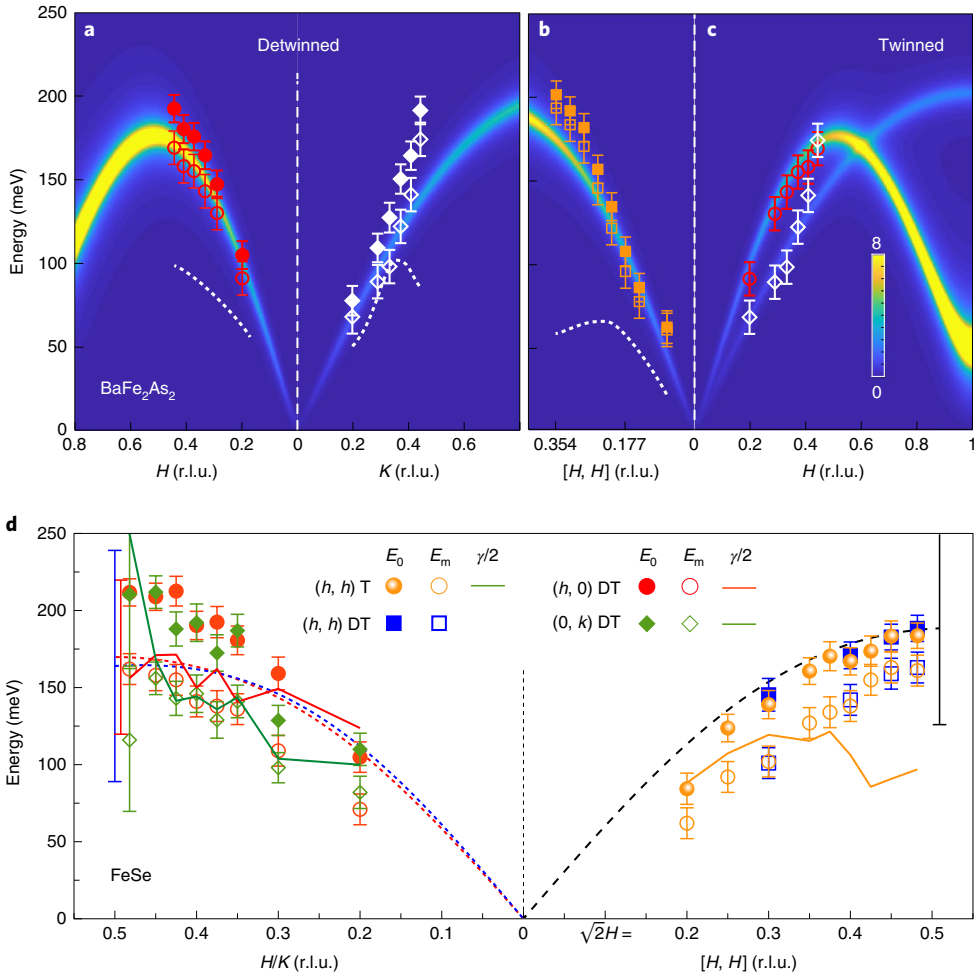

Fig. 3 | Energy dispersions and damping factors for the magnetic excitations of FeSe and $BaFe_2As_2$. a–c, Comparison between dispersions of the magnetic excitations measured with RIXS and a simulation with a Heisenberg model for detwinned (**a**) and twinned (**b**,**c**) $BaFe_2As_2$ (ref. [52]). The filled symbols, open symbols and white dashed curves in **a** and **b** are undamped energies (E_0), energies for the intensity maxima (E_m) and the damping factor ($\gamma/2$) fitted from the spectra shown in Fig. 2c,d with equation (1). The open symbols in **c** show E_m. **d**, Spin-excitation energy dispersions of FeSe obtained from the fitting of the RIXS spectra in Fig. 2a,b with equation (1). The filled (open) red circles, green diamonds, orange circles and blue squares mark the undamped energies E_0 (energies for intensity maxima E_m) of the dispersions along H (detwinned, DT), K (detwinned), $[H,H]$ (twinned, T) and $[H,H]$ (detwinned) directions, respectively. The red, green and orange lines mark the momentum-dependent damping factor $\gamma/2$ along the high-symmetry directions. The black, red and blue dashed curves are the calculated flavor-wave dispersions in the AFQ phase along the $[H,H]$ and H/K directions, respectively. The error bars for the data points are estimated according to the confidence interval of the fittings and the error in determining the $E=0$ position. The error bars mark the damping factor $\gamma/2$ along the corresponding directions.

based on an anisotropic Heisenberg $J_{1a}-J_{1b}-J_2$ model as described in ref. [52] (J_{1a} (J_{1b}) is the nearest-neighbour exchage interaction along a (b) axis. J_2 is the next-nearest-neighbour exchange interaction.), in which we set $L=0$ because the spin waves of $BaFe_2As_2$ are two-dimensional, especially for the high-energy spin excitations probed in our RIXS measurements. We find $E_0>\gamma/2$ at all the momenta measured, which indicates that the spin waves are underdamped and far from being critically damped. The intrinsic spin waves of the clearly resolved two different branches $S_h(q)$ and $S_k(q)$ around Γ are consistent with the anisotropic Heisenberg model, in which dispersive spin waves can only arise from the AF wave vector $\mathbf{Q}_1$ (S_1). The minor deviation of the branch $S_k(q)$ from the anisotropic Heisenberg model can be attributed to the failure of the anisotropic Heisenberg model in describing the small anisotropy of magnetic excitations at high energy, due to the emergence of the spin excitations around $\mathbf{Q}_2=(0,1)$ (S_2) at $E\gtrsim 100$ meV observed by neutron scattering[50,51]. Figure 3d shows the energy dispersion of FeSe obtained from the fitting of the magnetic excitations shown in Fig. 2a,b. The filled symbols mark the bare energy dispersion (E_0) without damping effect, and the open symbols represent the energy dispersion for the intensity maxima E_m.

The momentum-dependent damping factors $\gamma/2$ are overall larger than that for $BaFe_2As_2$, but still in the underdamped regime for most of the excitations. Moreover, the damping factor for S_{hh} (along the $[H,H]$ direction) is smaller than for $S_{h/k}$ in both FeSe and $BaFe_2As_2$, suggesting a common anisotropic damping effect in FeSC. The (anisotropic) underdamped nature of the magnetic excitations, not inferable in previous neutron scattering and RIXS studies on twinned samples[28,43], suggests that the excitations should arise from interacting local moments associated with strong electron correlations[53].

Because the largest momentum $(0.482,0)$ along H is close to the zone boundary $(0.5,0)$, the excitation energy scale of FeSe ($E_0\approx 200$ meV and $E_m\approx 160$ meV) at $(0.482,0)$ and $(0,0.482)$ (consistent with that in ref. [43]) reveals a much higher band top in the first Brillouin zone than that ($E\approx 120-150$ meV) observed by neutron scattering

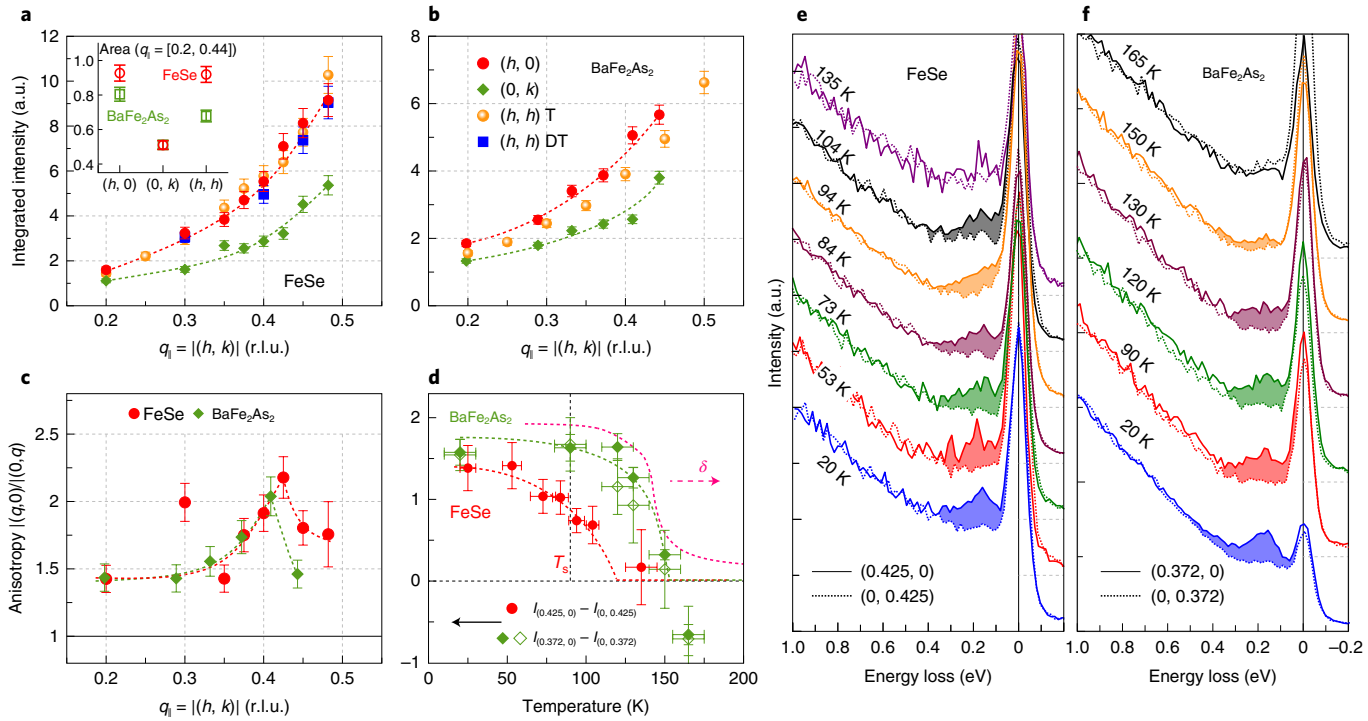

Fig. 4 | Anisotropic magnetic excitations in detwinned FeSe and $BaFe_2As_2$. **a**,**b**, Momentum-dependent energy-integrated intensity of magnetic excitations for FeSe (**a**) and $BaFe_2As_2$ (**b**). The inset shows the momentum-integrated intensity of $S_{h/k/hh}$ for FeSe (red circles) and $BaFe_2As_2$ (green squares) in the range of $q_\parallel = [0.2, 0.44]$. **c**, Spin excitation anisotropy between S_h and S_k, defined as the ratio between the integrated intensity for $(q, 0)$ and $(0, q)$ as shown in **a** and **b**. **d**, Temperature dependence of the spin-excitation difference between $S_h(q_\parallel)$ and $S_k(q_\parallel)$, in which the data points are the integrated intensity of $S_h(q_\parallel) - S_k(q_\parallel)$ in the energy range of [0.08, 0.4] eV, as shown in **e** and **f**. The dashed red and green lines in **c** and **d** are guides to the eye. The pink dashed curve shows the lattice distortion $\delta = (a-b)/(a+b)$ of $BaFe_2As_2$ under a uniaxial pressure of P~20 MPa, which reaches 0.36% below T~100 K. The vertical black dashed line marks the $T_s = 90$ K for FeSe. The vertical error bars in **a**–**d** are estimated from the data statistics and the confidence interval of the fittings, which determine the error bars in **c**. The horizontal bars in **d** mark the temperature range where data were collected. **e**,**f**, Temperature-dependent RIXS spectra for FeSe and $BaFe_2As_2$ measured at $q_\parallel = 0.425$ and 0.372, respectively. The shaded areas in **e** and **f** mark the intensity difference between $S_h(q_\parallel)$ and $S_k(q_\parallel)$.

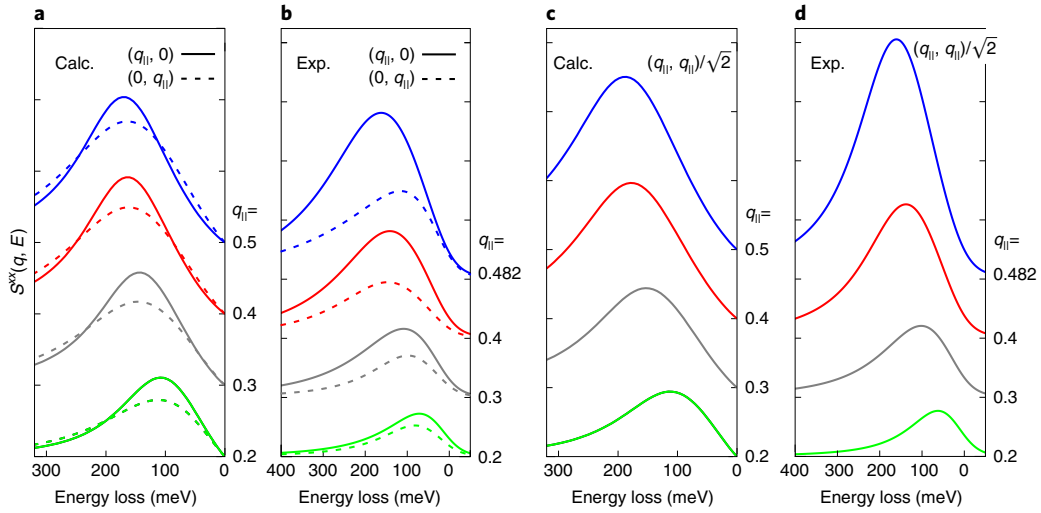

Fig. 5 | Calculated spin excitation spectra of the AFQ phase and their comparison with the fitting curve of the experimental $S(q_\parallel)$ from RIXS. **a**,**c**, Calculated spectra along the H/K directions (**a**) and the $[H, H]$ direction (**c**). **b**,**d**, Fitting curves of the experimental $S(q_\parallel)$ along the H/K directions (**b**) and $[H, H]$ direction (**d**).

in the Brillouin zone around (1,0)[28]. This is in stark contrast to the case of $BaFe_2As_2$, where the dispersions measured by RIXS and neutron scattering can be consistently described with one model (Fig. 2)[39,50]. We attribute this difference to the absence of stripe AF order in FeSe. Because of the translational symmetry of the stripe AF order ($\mathbf{k} = (1,0)$) in $BaFe_2As_2$, the magnetic excitations in the

first Brillouin zone can be deemed as a replica of the ones in the Brillouin zone centring at $\mathbf{Q}=(1,0)$. However, long-range AF order is not established in spite of the strong in-plane magnetic correlations in FeSe. Accordingly, the dispersions around Γ and (1,0) do not have to be identical. However, how to quantitatively reconcile the neutron scattering and RIXS results is still an open question.

Figure 4a,b shows the momentum-dependent energy-integrated intensity of the spin excitations S_h, S_k and S_{hh} for FeSe and $BaFe_2As_2$, respectively. With increasing $q_\parallel$, the integrated intensities along all three high-symmetry directions increase monotonically. The spin-excitation intensity for FeSe is slightly higher than for $BaFe_2As_2$, qualitatively consistent with previous neutron scattering results[28]. Note the momentum-direction dependence of the amplitude for $S_{h/k/hh}$ is modulated by the anisotropic damping factor inherent to $S_{1,2}$, which requires $S_{1,2}=0$ at Γ (ref. [52]). To quantify the spin-excitation anisotropy, we plotted the ratio $I_{(q,0)}/I_{(0,q)}=S_h/S_k$ for FeSe and $BaFe_2As_2$ in the same panel (Fig. 4c). It is surprising that the spin-excitation anisotropy of FeSe (reflecting the nematic spin correlations) is rather similar to the spin-wave anisotropy of $BaFe_2As_2$ in both amplitude and energy scale. Furthermore, in the high-energy/momentum region, the anisotropy of FeSe is even larger than for $BaFe_2As_2$. This prominent spin-excitation anisotropy signifies strong electronic nematicity with large energy scale ($E\approx 200$ meV) and magnitude in FeSe. Moreover, the temperature dependence of the difference between S_h and S_k for FeSe at selected $q_\parallel=0.425$ decreases with increasing temperature, persists to a temperature (104 K) 20% higher than T_s and finally drastically reduces at a temperature (135 K) well above T_s, indicating a gradual suppression of nematic spin correlations above T_s (Fig. 4d,e). Because FeSe is under uniaxial strain applied from the $BaFe_2As_2$ substrate (pink dashed curve, Fig. 4d), T_s is no longer well defined. For this reason, it is not surprising that the spin-excitation anisotropy disappears at a temperature above the zero-pressure T_s. This temperature dependence is similar to that for $BaFe_2As_2$, as shown in Fig. 4d,f, where the anisotropy at $q_\parallel=0.372$ persists at a temperature slightly higher than T_N but vanishes at $T=165$ K.

Previous measurements of the spin dynamics in detwinned FeSe were constrained to low energies ($E\lesssim 10$ meV)[35] and were unable to discriminate between the different scenarios for the nematicity in FeSe. Our present measurements over a large energy window enable the discovery that the detwinned FeSe harbours high-energy (up to 200 meV) anisotropic spin excitations that are dispersive and underdamped. This surprising finding appears to be at variance with the itinerant mechanism for the nematicity in FeSe. In the itinerant picture, the leading contribution to the spin excitation spectrum comes from a two-particle process, that is, a convolution of single-electron and single-hole excitations. Because of this particle–hole nature of the spin excitations, damping already appears in the leading-order contribution to the spectrum. This Landau damping means that the leading-order contribution to the spin excitations is generically already overdamped; higher-order processes further enhance the damping. An itinerant model calculation indeed shows that the spin excitations at such pertinent (high) energies are highly overdamped[54]. Our work is expected to motivate further studies on this issue within the itinerant description.

Instead, the dispersive and underdamped nature of the high-energy spin excitations point to a local-moment starting point to describe the nematicity. Taking together that the energy scale of the spin-excitation anisotropy is far beyond the d_{xz}/d_{yz} orbital splitting ($E\approx 50$ meV), and the nematic spin correlations decrease and finally disappear at a temperature above T_s, we conclude that the nematicity is probably spin-driven.

This has led us to consider a generalized bilinear–biquadratic model on a square lattice with local moments[31]. Here, the local moments capture the majority of the spin degrees of freedom, especially at high energies. Indeed, the importance of electron correlations in iron-based superconductors has been clearly demonstrated in recent years. Although several specific theoretical approaches have been taken to address the effect of electron correlations, including Hund's metal[55], proximity to an orbital-selective Mott phase[6,56] and a Mott–Hund's picture[57], they share the common feature that the single-electron states have a mixture of incoherent and coherent states (which dominate at high and low energies, respectively). Indeed, for FeSe, ARPES has directly observed the high-energy Hubbard bands[58,59], which mediate effective exchange interactions between quasi-localized moments[60].

In the generalized bilinear–biquadratic model, the leading-order contributions to the spin excitation spectrum comprise a one-particle process. Because only sub-leading contributions that involve more-than-one-particle processes contribute to damping, the high-energy spin excitations are underdamped. More specifically, we have calculated the spin dynamics in the proposed picture for the nematicity based on a (1,0) antiferroquadrupolar state using the flavor-wave method[31]. This approach treats the spin dipolar and quadrupolar excitations on an equal footing, as the bosonic flavor waves. Consistent with the physical picture, the spin-excitation spectrum is dispersive and underdamped (for details see the Supplementary Information). In Fig. 5 we show that the calculated spin dynamics provide a good understanding of the experimental data. Thus, our results provide evidence for a local-moment-based picture for the nematicity of FeSe.

The rich properties of the Fe-based superconductors in general and nematic FeSe in particular have been addressed from both weak[5,37,61] and strong[6,30,31] coupling perspectives, with each having had successes. Our work brings about a hitherto unknown and remarkable feature of universality across the Fe-based superconductors. For $BaFe_2As_2$ with collinear AF order, the anisotropy can be readily interpreted in the picture of intrinsic spin waves[50,51]. FeSe, by contrast, lacks long-range magnetic order even though it is nematic. The local-moment-based understanding, as dictated by the qualitative similarities in the high-energy spin excitations of FeSe and $BaFe_2As_2$, suggests that the largest spin spectral weight in both the iron chalcogenides and pnictides is associated with the incoherent electronic excitations induced by the underlying electron correlations. As such, our work not only allows for discriminating the proposed mechanisms for the nematicity of FeSe, but also points to a unified understanding of the correlation physics[42] across the seemingly distinct classes of Fe-based superconductors.

Online content

Any methods, additional references, Nature Research reporting summaries, source data, extended data, supplementary information, acknowledgements, peer review information; details of author contributions and competing interests; and statements of data and code availability are available at https://doi.org/10.1038/s41567-022-01603-1.

Received: 1 August 2021; Accepted: 31 March 2022;
Published online: 19 May 2022

References

1. Fradkin, E., Kivelson, S. A. & Tranquada, J. M. Colloquium: theory of intertwined orders in high temperature superconductors. *Rev. Mod. Phys.* **87**, 457–482 (2015).
2. Chu, J.-H. et al. In-plane resistivity anisotropy in an underdoped iron arsenide superconductor. *Science* **329**, 824–826 (2010).
3. Yi, M. et al. Symmetry-breaking orbital anisotropy observed for detwinned \ $Ba(Fe_{1-x}Co_x)_2As_2$ above the spin density wave transition. *Proc. Natl Acad. Sci. USA* **108**, 6878–6883 (2011).
4. Chu, J.-H., Kuo, H.-H., Analytis, J. G. & Fisher, I. R. Divergent nematic susceptibility in an iron arsenide superconductor. *Science* **337**, 710–712 (2012).
5. Fernandes, R. M., Chubukov, A. V. & Schmalian, J. What drives nematic order in iron-based superconductors? *Nat. Phys.* **10**, 97–104 (2014).

6. Si, Q., Yu, R. & Abrahams, E. High temperature superconductivity in iron pnictides and chalcogenides. *Nat. Rev. Mater.* **1**, 16017 (2016).
7. Kuo, H.-H., Chu, J.-H., Palmstrom, J. C., Kivelson, S. A. & Fisher, I. R. Ubiquitous signatures of nematic quantum criticality in optimally doped Fe-based superconductors. *Science* **352**, 958–962 (2016).
8. Böhmer, A. E. & Meingast, C. Electronic nematic susceptibility of iron-based superconductors. *C. R. Phys.* **17**, 90–112 (2016).
9. Böhmer, A. E. & Kreisel, A. Nematicity, magnetism and superconductivity in FeSe. *J. Phys. Condens. Matter* **30**, 023001 (2018).
10. Metlitski, M. A. et al. Cooper pairing in non-Fermi liquids. *Phys. Rev. B* **91**, 115111 (2015).
11. Lederer, S. et al. Enhancement of superconductivity near a nematic quantum critical point. *Phys. Rev. Lett.* **114**, 097001 (2015).
12. Eckberg, C. et al. Sixfold enhancement of superconductivity in a tunable electronic nematic system. *Nat. Phys.* **16**, 346–350 (2020).
13. Hsu, F. C. et al. Superconductivity in the PbO-type structure α-FeSe. *Proc. Natl Acad. Sci. USA* **105**, 14262–14264 (2008).
14. McQueen, T. M. et al. Tetragonal-to-orthorhombic structural phase transition at 90 K in the superconductor $Fe_{1.01}Se$. *Phys. Rev. Lett.* **103**, 057002 (2009).
15. Tanatar, M. A. et al. Origin of resistivity anisotropy in the nematic phase of FeSe. *Phys. Rev. Lett.* **117**, 127001 (2016).
16. Coldea, A. & Watson, M. D. The key ingredients of the electronic structure of FeSe. *Annu. Rev. Condens. Matter Phys.* **9**, 125–146 (2018).
17. Liu, D. F. et al. Orbital origin of extremely anisotropic superconducting gap in nematic phase of FeSe superconductor. *Phys. Rev. X* **8**, 031033 (2018).
18. Hashimoto, T. et al. Superconducting gap anisotropy sensitive to nematic domains in FeSe. *Nat. Commun.* **9**, 282 (2018).
19. Rhodes, L. C. et al. Scaling of the superconducting gap with orbital character in FeSe. *Phys. Rev. B* **98**, 180503(R) (2018).
20. Sprau, P. O. et al. Discovery of orbital-selective Cooper pairing in FeSe. *Science* **357**, 75–80 (2017).
21. Lee, C. C., Yin, W.-G. & Ku, W. Ferro-orbital order and strong magnetic anisotropy in the parent compounds of iron-pnictide superconductors. *Phys. Rev. Lett.* **103**, 267001 (2009).
22. Yi, M. et al. The nematic energy scale and the missing electron pocket in FeSe. *Phys. Rev. X* **9**, 041049 (2019).
23. Baek, S.-H. et al. Orbital-driven nematicity in FeSe. *Nat. Mater.* **14**, 210–214 (2015).
24. Böhmer, A. E. et al. Origin of the tetragonal-to-orthorhombic phase transition in FeSe: a combined thermodynamic and NMR study of nematicity. *Phys. Rev. Lett.* **114**, 027001 (2015).
25. Yamakawa, Y., Onari, S. & Kontani, H. Nematicity and magnetism in FeSe and other families of Fe-based superconductors. *Phys. Rev. X* **6**, 021032 (2016).
26. Onari, S., Yamakawa, Y. & Kontani, H. Sign-reversing orbital polarization in the nematic phase of FeSe due to the C_2 symmetry breaking in the self-energy. *Phys. Rev. Lett.* **116**, 227001 (2016).
27. Wang, Q. et al. Strong interplay between stripe spin fluctuations, nematicity and superconductivity in FeSe. *Nat. Mater.* **15**, 159–163 (2016).
28. Wang, Q. et al. Magnetic ground state of FeSe. *Nat. Commun.* **7**, 12182 (2016).
29. Ma, M. W. et al. Prominent role of spin-orbit coupling in FeSe revealed by inelastic neutron scattering. *Phys. Rev. X* **7**, 021025 (2017).
30. Wang, F., Kivelson, S. & Lee, D.-H. Nematicity and quantum paramagnetism in FeSe. *Nat. Phys.* **11**, 959–963 (2015).
31. Yu, R. & Si, Q. Antiferroquadrupolar and Ising-nematic orders of a frustrated bilinear-biquadratic Heisenberg model and implications for the magnetism of FeSe. *Phys. Rev. Lett.* **115**, 116401 (2015).
32. Glasbrenner, J. K. et al. Effect of magnetic frustration on nematicity and superconductivity in iron chalcogenides. *Nat. Phys.* **11**, 953–958 (2015).
33. She, J.-H., Lawler, M. J. & Kim, E.-A. Quantum spin liquid intertwining nematic and superconducting order in FeSe. *Phys. Rev. Lett.* **121**, 237002 (2018).
34. Lu, X. et al. Nematic spin correlations in the tetragonal state of uniaxial-strained $BaFe_{2-x}Ni_xAs_2$. *Science* **345**, 657–660 (2014).
35. Chen, T. et al. Anisotropic spin fluctuations in detwinned FeSe. *Nat. Mater.* **18**, 709–716 (2019).
36. Yu, R., Zhu, J.-X. & Si, Q. Orbital-selective superconductivity, gap anisotropy and spin resonance excitations in a multiorbital t-J_1-J_2 model for iron pnictides. *Phys. Rev. B* **89**, 024509 (2014).
37. Fanfarillo, L. et al. Orbital-dependent Fermi surface shrinking as a fingerprint of nematicity in FeSe. *Phys. Rev. B* **94**, 155138 (2016).
38. Tian, L. et al. Spin fluctuation anisotropy as a probe of orbital-selective hole-electron quasiparticle excitations in detwinned $Ba(Fe_{1-x}Co_x)_2As_2$. *Phys. Rev. B* **100**, 134509 (2019).
39. Zhou, K. et al. Persistent high-energy spin excitations in iron-pnictide superconductors. *Nat. Commun.* **4**, 1470 (2013).
40. Pelliciari, J. et al. Local and collective magnetism of $EuFe_2As_2$. *Phys. Rev. B* **95**, 115152 (2017).
41. Garcia, F. A. et al. Anisotropic magnetic excitations and incipient Néel order in $Ba(Fe_{1-x}Mn_x)_2As_2$. *Phys. Rev. B* **99**, 115118 (2019).
42. Pelliciari, J. et al. Reciprocity between local moments and collective magnetic excitations in the phase diagram of $BaFe_2(As_{1-x}P_x)_2$. *Commun. Phys.* **2**, 139 (2019).
43. Rahn, M. C. et al. Paramagnon dispersion in β-FeSe observed by Fe L-edge resonant inelastic X-ray scattering. *Phys. Rev. B* **99**, 014505 (2019).
44. Pelliciari, J. et al. Evolution of spin excitations from bulk to monolayer FeSe. *Nat. Commun.* **12**, 3122 (2021).
45. Ament, L. J. P. et al. Resonant inelastic X-ray scattering studies of elementary excitations. *Rev. Mod. Phys.* **83**, 705–767 (2011).
46. Schlappa, J. et al. Spin–orbital separation in the quasi-one-dimensional Mott insulator Sr_2CuO_3. *Nature* **485**, 82–85 (2012).
47. Peng, Y. Y. et al. Influence of apical oxygen on the extent of in-plane exchange interaction in cuprate superconductors. *Nat. Phys.* **13**, 1201–1206 (2017).
48. Jia, C. et al. Using RIXS to uncover elementary charge and spin excitations. *Phys. Rev. X* **6**, 021020 (2016).
49. Hepting, M. et al. Three-dimensional collective charge excitations in electron-doped copper oxide superconductors. *Nature* **563**, 374–378 (2018).
50. Lu, X. et al. Spin waves in detwinned $BaFe_2As_2$. *Phys. Rev. Lett.* **121**, 067002 (2018).
51. Liu, C. et al. Anisotropic magnetic excitations of a frustrated bilinear-biquadratic spin model—implications for spin waves of detwinned iron pnictides. *Phys. Rev. B* **101**, 024510 (2020).
52. Harriger, L. W. et al. Nematic spin fluid in the tetragonal phase of $BaFe_2As_2$,. *Phys. Rev. B* **84**, 054544 (2011).
53. Wang, M. et al. Doping dependence of spin excitations and its correlations with high-temperature superconductivity in iron pnictides. *Nat. Commun.* **4**, 2874 (2013).
54. Kreisel, A., Andersen, B. M. & Hirschfeld, P. J. Itinerant approach to magnetic neutron scattering of FeSe: effect of orbital selectivity. *Phys. Rev. B* **98**, 214518 (2019).
55. Fernandes, R. M. et al. Iron pnictides and chalcogenides: a new paradigm for superconductivity. *Nature* **601**, 39–44 (2022).
56. Yu, R., Hu, H., Nica, E. M., Zhu, J.-X. & Si, Q. Orbital selectivity in electron correlations and superconducting pairing of iron-based superconductors. *Front. Phys.* **9**, 978347 (2021).
57. Lafuerza, S. et al. Evidence of Mott physics in iron pnictides from X-ray spectroscopy. *Phys. Rev. B* **96**, 045133 (2017).
58. Watson, M. D. et al. Formation of Hubbard-like bands as a fingerprint of strong electron-electron interactions in FeSe. *Phys. Rev. B* **95**, 081106(R) (2017).
59. Evtushinsky, D. V. et al. Direct observation of dispersive lower Hubbard band in iron-based superconductor FeSe. Preprint at https://arxiv.org/abs/1612.02313 (2016).
60. Ding, W., Yu, R., Si, Q. & Abrahams, E. Effective exchange interactions for bad metals and implications for iron-based superconductors. *Phys. Rev. B* **100**, 235113 (2019).
61. Mukherjee, S., Kreisel, A., Hirschfeld, P. J. & Andersen, B. M. Model of electronic structure and superconductivity in orbitally ordered FeSe. *Phys. Rev. Lett.* **115**, 026402 (2015).

Methods

Sample preparation. The high-quality $BaFe_2As_2$ and FeSe single crystals used in the present study were grown using self-flux and the chemical vapour transport method, respectively. The $BaFe_2As_2$ single crystals were oriented using a Laue camera and cut along the tetragonal [110] and [1–10] directions using a high-precision wire saw (WS-25). The directions of the self-cleaved edges of the FeSe single crystals were also determined using a Laue camera. The well-cut $BaFe_2As_2$ crystals, with typical dimensions of 5 mm × 4.3 mm × 0.5 mm, were pre-cleaved before the final preparation. For RIXS measurements of $BaFe_2As_2$, we placed a ceramic top post onto the upper surface of $BaFe_2As_2$ for in situ cleaving. For RIXS measurements of FeSe, we glued thin FeSe crystals onto the upper surface of $BaFe_2As_2$ along the same direction using epoxy Stycast 1266 and a small ceramic top post onto the surface of the FeSe. The prepared crystals with the posts were inserted into the slot of the uniaxial-pressure devices, which were mounted on a modified copper sample holder of the RIXS spectrometer (Fig. 1b)[62].

Experimental set-ups. The RIXS and XAS measurements were performed with the RIXS spectrometer at the ADRESS beamline of the Swiss Light Source at the Paul Scherrer Institut[63,64]. The beam size at the sample position was $4 \times 55\,\mu m^2$. All the measurements shown in the main text were collected using linear horizontal (LH) polarization (electric field vector of the incident photons lying within the horizontal scattering plane), denoted as π polarization. The RIXS spectra were collected with a grazing-incidence configuration, as shown in Fig. 1d. The scattering angle was set to $2\theta_s = 130°$, with which a substantial area of the first Brillouin zone is accessible (Fig. 1d, grey circle). The measurements were performed along high-symmetry directions H/K and $[H,H]$ in orthorhombic notation. The total energy resolution for the RIXS measurements was set to 80 meV. The in-plane momentum $q_{\parallel}$ could be tuned continuously by rotating the sample and thereby changing the angle δ. Before the measurements, the sample holder was inserted into the manipulator head and the top post was removed by cleaving at low temperature (~20 K) and in ultrahigh vacuum ($<10^{-10}$ mbar). We defined the wave vector $\mathbf{Q}$ in reciprocal space as $\mathbf{Q} = H\mathbf{a}^* + K\mathbf{b}^* + L\mathbf{c}^*$, where H, K, L are Miller indices and $\mathbf{a}^* = \hat{\mathbf{a}}2\pi/a_o$, $\mathbf{b}^* = 2\pi/b_o$, and $\mathbf{c}^* = 2\pi/c$ are reciprocal lattice unit vectors with $a_o \approx 5.334$ Å, $b_o \approx 5.308$ Å and $c \approx 5.486$ Å. The FeSe tri-layer height was $d \approx 5.5$ Å. The orthorhombic lattice distortion of FeSe was $\delta = (a_o - b_o)/(a_o + b_o) \approx 0.27\%$ at a temperature well below T_s.

Data availability

All data that support the plots in this paper are available from the corresponding author upon reasonable request. Source data are provided with this paper. The data can also be found at Figshare public repository[65].

Code availability

All relevant source code is available from the corresponding author upon reasonable request.

References

62. Wang, Q. et al. Uniaxial pressure induced stripe order rotation in $La_{1.88}Sr_{0.12}CuO_4$. *Nat. Commun.* **13**, 1795 (2022).
63. Strocov, V. N. et al. High-resolution soft X-ray beamline ADRESS at the Swiss Light Source for resonant inelastic X-ray scattering and angle-resolved photoelectron spectroscopies. *J. Synchrotron Radiat.* **17**, 631–643 (2010).
64. Ghiringhelli, G. et al. A high resolution spectrometer for resonant X-ray emission in the 400–1,600-eV energy range. *Rev. Sci. Instrum.* **77**, 113108 (2006).
65. Lu, X et al. Spin-excitation anisotropy in the nematic state of detwinned FeSe. https://figshare.com/articles/dataset/Spinexcitation_anisotropy_in_the_nematic_state_of_detwinned_FeSe/19382825 (2022).

Acknowledgements

The work at Beijing Normal University is supported by National Key Projects for Research and Development of China with Grant No. 2021YFA1400400 and the National Natural Science Foundation of China (grants nos. 11922402 and 11734002;) (X.L.). The RIXS experiments were carried out at the ADRESS beamline of the Swiss Light Source at the Paul Scherrer Institut (PSI). The work at PSI is supported by the Swiss National Science Foundation through project no. 200021_178867 and the Sinergia network Mott Physics Beyond the Heisenberg Model (MPBH; projects nos. CRSII2 160765/1 and CRSII2 141962; T.S.). The work at Renmin University was supported by the Ministry of Science and Technology of China, National Program on Key Research Project grant no. 2016YFA0300504 and Research Funds of Remnin University of China grant no. 18XNLG24 (R.Y.). The experimental work at Rice University is supported by the US Department of Energy, Basic Energy Sciences, under grant no. DE-SC0012311 (P.D.). The single-crystal synthesis work at Rice is supported by the Robert A. Welch Foundation grant no. C-1839 (P.D.). The theoretical work at Rice was supported by the US Department of Energy, Office of Science, Basic Energy Sciences, under award no. DE-SC0018197, and the computational part by the Robert A. Welch Foundation grant no. C-1411 (Q.S.). Q.S. acknowledges the hospitality of the Aspen Center for Physics, which is supported by NSF grant no. PHY-1607611.

Author contributions

X.L. conceived this project and developed the detwinning strategy. X.L. and T.S. wrote the beamtime proposals and coordinated the experiments as well as all other project phases. X.L., W.Z., Y.T., E.P., R.L., Z.T. and T.S. carried out the RIXS experiments with the support of V.N.S. X.L. analysed the data with assistance from Y.S. P.L., R.L. and Z.T. prepared the $BaFe_2As_2$ single crystals. T.C. and P.D. provided the FeSe single crystals. R.Y. and Q.S. carried out theoretical and computational analyses. X.L., P.D. and T.S. wrote the manuscript with input from R.Y. and Q.S. All authors made comments.

Competing interests

The authors declare no competing interests.

Additional information

Supplementary information The online version contains supplementary material available at https://doi.org/10.1038/s41567-022-01603-1.

Correspondence and requests for materials should be addressed to Xingye Lu, Pengcheng Dai or Thorsten Schmitt.

Peer review information *Nature Physics* thanks the anonymous reviewers for their contribution to the peer review of this work